

Light Propagation with Phase Discontinuities: Generalized Laws of Reflection and Refraction

Nanfang Yu,¹ Patrice Genevet,^{1,2} Mikhail A. Kats,¹ Francesco Aieta,^{1,3} Jean-Philippe Tetienne,^{1,4} Federico Capasso,^{1,*} Zeno Gaburro^{1,5*}

Conventional optical components rely on gradual phase shifts accumulated during light propagation to shape light beams. New degrees of freedom are attained by introducing abrupt phase changes over the scale of the wavelength. A two-dimensional array of optical resonators with spatially varying phase response and subwavelength separation can imprint such phase discontinuities on propagating light as it traverses the interface between two media. Anomalous reflection and refraction phenomena are observed in this regime in optically thin arrays of metallic antennas on silicon with a linear phase variation along the interface, which are in excellent agreement with generalized laws derived from Fermat's principle. Phase discontinuities provide great flexibility in the design of light beams, as illustrated by the generation of optical vortices through use of planar designer metallic interfaces.

The shaping of the wavefront of light with optical components such as lenses and prisms, as well as diffractive elements such as gratings and holograms, relies on gradual phase changes accumulated along the optical path. This approach is generalized in transformation optics (1, 2), which uses metamaterials to bend light in unusual ways, achieving such phenomena as negative refraction, subwavelength-focusing, and cloaking (3, 4) and even to explore unusual geometries of space-time in the early universe (5). A new degree of freedom of controlling wavefronts can be attained by introducing abrupt phase shifts over the scale of the wavelength along the optical path, with the propagation of light governed by Fermat's principle. The latter states that the trajectory taken between two points A and B by a ray of light is that of the least optical path, $\int_A^B n(\vec{r}) dr$, where $n(\vec{r})$ is the local index of refraction, and readily gives the laws of reflection and refraction between two media. In its most general form, Fermat's principle can be stated as the principle of stationary phase (6–8); that is, the derivative of the phase $\int_A^B d\varphi(\vec{r})$ accumulated along the actual light path will be zero with respect to infinitesimal variations of the path. We show that an abrupt phase shift $\Phi(\vec{r}_s)$ over the scale of the wavelength can be introduced in the optical path by suitably engineering the interface

between two media; $\Phi(\vec{r}_s)$ depends on the coordinate \vec{r}_s along the interface. Then, the total phase shift $\Phi(\vec{r}_s) + \int_A^B \vec{k} \cdot d\vec{r}$ will be stationary for the actual path that light takes; \vec{k} is the wave vector of the propagating light. This provides a generalization of the laws of reflection and refraction, which is applicable to a wide range of subwavelength structured interfaces between two media throughout the optical spectrum.

Generalized laws of reflection and refraction.

The introduction of an abrupt phase shift, denoted as phase discontinuity, at the interface between two media allows us to revisit the laws of reflection and refraction by applying Fermat's principle. Consider an incident plane wave at an angle θ_i . Assuming that the two paths are infinitesimally close to the actual light path (Fig. 1), then the phase difference between them is zero

$$\begin{aligned} [k_o n_i \sin(\theta_i) dx + (\Phi + d\Phi)] - \\ [k_o n_t \sin(\theta_t) dx + \Phi] = 0 \end{aligned} \quad (1)$$

where θ_t is the angle of refraction; Φ and $\Phi + d\Phi$ are, respectively, the phase discontinuities at the locations where the two paths cross the interface; dx is the distance between the crossing points; n_i and n_t are the refractive indices of the two media; and $k_o = 2\pi/\lambda_o$, where λ_o is the vacuum wavelength. If the phase gradient along the interface is designed to be constant, the previous equation leads to the generalized Snell's law of refraction

$$\sin(\theta_t) n_t - \sin(\theta_i) n_i = \frac{\lambda_o}{2\pi} \frac{d\Phi}{dx} \quad (2)$$

Equation 2 implies that the refracted beam can have an arbitrary direction, provided that a suitable constant gradient of phase discontinuity along the interface ($d\Phi/dx$) is introduced. Because of the nonzero phase gradient in this modified Snell's law, the two angles of incidence $\pm\theta_i$ lead to different values for the angle of refraction. As a consequence, there are two possible critical an-

gles for total internal reflection, provided that $n_t < n_i$:

$$\theta_c = \arcsin\left(\pm \frac{n_t}{n_i} - \frac{\lambda_o}{2\pi n_i} \frac{d\Phi}{dx}\right) \quad (3)$$

Similarly, for reflection we have

$$\sin(\theta_r) - \sin(\theta_i) = \frac{\lambda_o}{2\pi n_i} \frac{d\Phi}{dx} \quad (4)$$

where θ_r is the angle of reflection. There is a nonlinear relation between θ_r and θ_i , which is markedly different from conventional specular reflection. Equation 4 predicts that there is always a critical angle of incidence

$$\theta'_c = \arcsin\left(1 - \frac{\lambda_o}{2\pi n_i} \left| \frac{d\Phi}{dx} \right| \right) \quad (5)$$

above which the reflected beam becomes evanescent.

In the above derivation, we have assumed that Φ is a continuous function of the position along the interface; thus, all the incident energy is transferred into the anomalous reflection and refraction. However, because experimentally we use an array of optically thin resonators with subwavelength separation to achieve the phase change along the interface, this discreteness implies that there are also regularly reflected and refracted beams, which follow conventional laws of reflection and refraction ($d\Phi/dx = 0$ in Eqs. 2 and 4). The separation between the resonators controls the amount of energy in the anomalously reflected and refracted beams. We have also assumed that the amplitudes of the scattered radiation by each resonator are identical, so that the reflected and refracted beams are plane waves. In the next section, we will show with simulations—which represent numerical solutions of Maxwell's

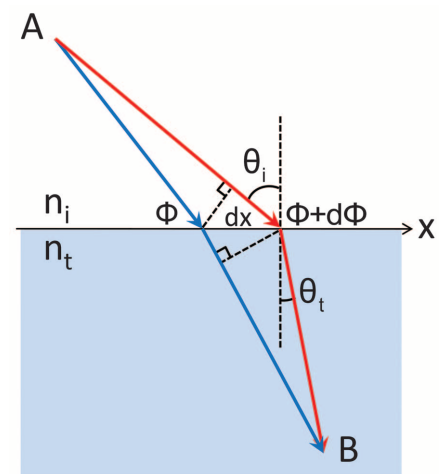


Fig. 1. Schematics used to derive the generalized Snell's law of refraction. The interface between the two media is artificially structured in order to introduce an abrupt phase shift in the light path, which is a function of the position along the interface. Φ and $\Phi + d\Phi$ are the phase shifts where the two paths (blue and red) cross the boundary.

¹School of Engineering and Applied Sciences, Harvard University, Cambridge, MA 02138, USA. ²Institute for Quantum Studies and Department of Physics, Texas A&M University, College Station, TX 77843, USA. ³Dipartimento di Fisica e Ingegneria dei Materiali e del Territorio, Università Politecnica delle Marche, via Brecce Bianche, 60131 Ancona, Italy. ⁴Laboratoire de Photonique Quantique et Moléculaire, Ecole Normale Supérieure de Cachan and CNRS, 94235 Cachan, France. ⁵Dipartimento di Fisica, Università degli Studi di Trento, via Sommarive 14, 38100 Trento, Italy.

*To whom correspondence should be addressed. E-mail: capasso@seas.harvard.edu (F.C.); gaburro@seas.harvard.edu (Z.G.)

equations—how, indeed, one can achieve the equal-amplitude condition and the constant phase gradient along the interface through suitable design of the resonators.

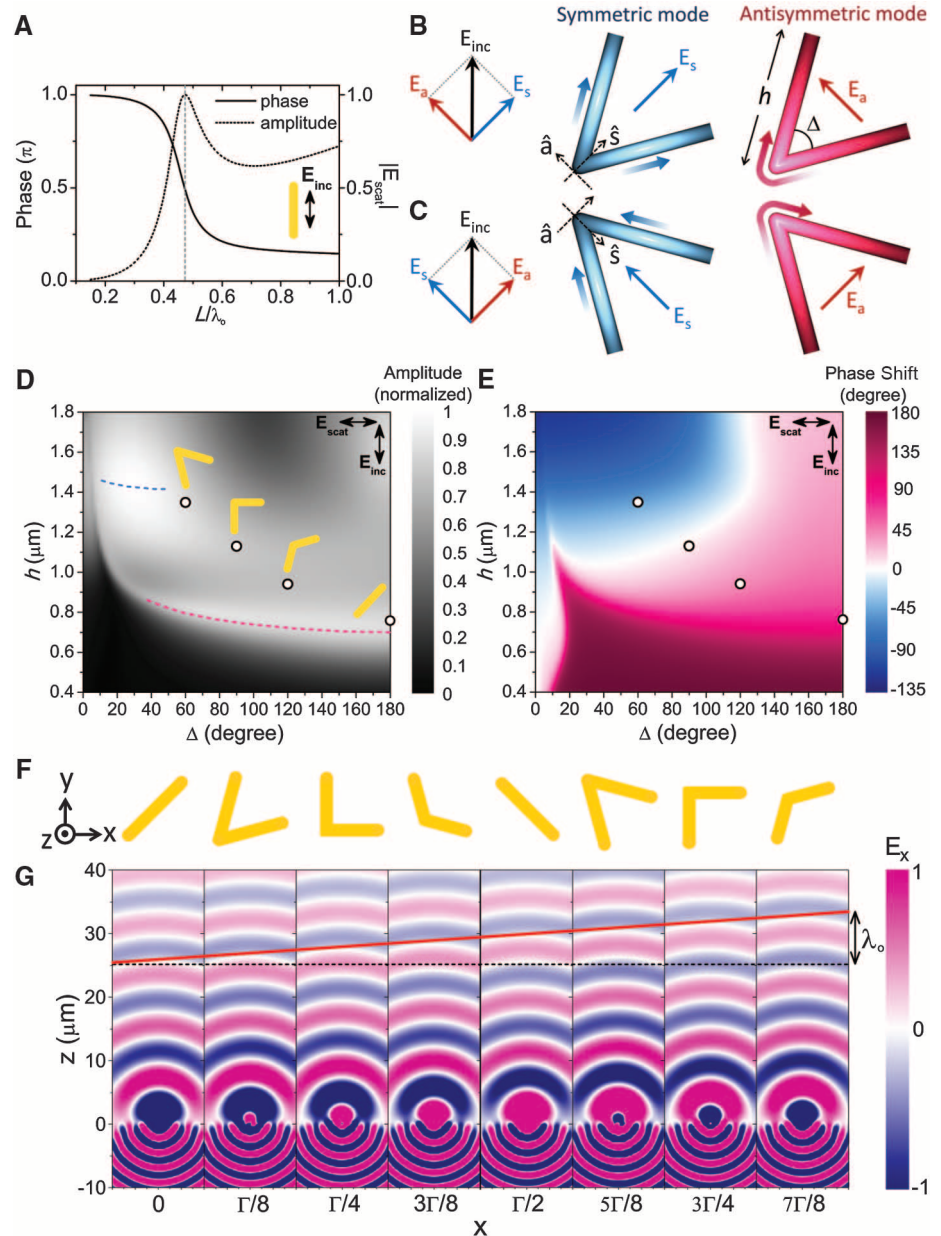
There is a fundamental difference between the anomalous refraction phenomena caused by phase discontinuities and those found in bulk designer metamaterials, which are caused by either negative dielectric permittivity and negative magnetic permeability or anisotropic dielectric permittivity with different signs of permittivity tensor components along and transverse to the surface (3, 4).

Phase response of optical antennas. The phase shift between the emitted and the incident radiation of an optical resonator changes appreciably

across a resonance. By spatially tailoring the geometry of the resonators in an array and hence their frequency response, one can design the phase discontinuity along the interface and mold the wavefront of the reflected and refracted beams in nearly arbitrary ways. The choice of the resonators is potentially wide-ranging, from electromagnetic cavities (9, 10) to nanoparticle clusters (11, 12) and plasmonic antennas (13, 14). We concentrated on the latter because of their widely tailorable optical properties (15–19) and the ease of fabricating planar antennas of nanoscale thickness. The resonant nature of a rod antenna made of a perfect electric conductor is shown in Fig. 2A (20).

Phase shifts covering the 0-to- 2π range are needed to provide full control of the wavefront. To achieve the required phase coverage while maintaining large scattering amplitudes, we used the double-resonance properties of V-shaped antennas, which consist of two arms of equal length h connected at one end at an angle Δ (Fig. 2B). We define two unit vectors to describe the orientation of a V-antenna: \hat{s} along the symmetry axis of the antenna and \hat{a} perpendicular to \hat{s} (Fig. 2B). V-antennas support “symmetric” and “antisymmetric” modes (Fig. 2B, middle and right), which are excited by electric-field components along \hat{s} and \hat{a} axes, respectively. In the symmetric mode, the current distribution in each arm approximates

Fig. 2. (A) Calculated phase and amplitude of scattered light from a straight rod antenna made of a perfect electric conductor (20). The vertical dashed line indicates the first-order dipolar resonance of the antenna. **(B)** A V-antenna supports symmetric and antisymmetric modes, which are excited, respectively, by components of the incident field along \hat{s} and \hat{a} axes. The angle between the incident polarization and the antenna symmetry axis is 45° . The schematic current distribution is represented by colors on the antenna (blue for symmetric and red for antisymmetric mode), with brighter color representing larger currents. The direction of current flow is indicated by arrows with color gradient. **(C)** V-antennas corresponding to mirror images of those in (B). The components of the scattered electric field perpendicular to the incident field in (B) and (C) have a π phase difference. **(D)** and **(E)** Analytically calculated amplitude and phase shift of the cross-polarized scattered light for V-antennas consisting of gold rods with a circular cross section and with various length h and angle between the rods Δ at $\lambda_0 = 8 \mu\text{m}$ (20). The four circles in (D) and (E) indicate the values of h and Δ used in experiments. The rod geometry enables analytical calculations of the phase and amplitude of the scattered light, without requiring the extensive numerical simulations needed to compute the same quantities for “flat” antennas with a rectangular cross-section, as used in the experiments. The optical properties of a rod and “flat” antenna of the same length are quantitatively very similar, when the rod antenna diameter and the “flat” antenna width and thickness are much smaller than the length (20). **(F)** Schematic unit cell of the plasmonic interface for demonstrating the generalized laws of reflection and refraction. The sample shown in Fig. 3A is created by periodically translating in the x - y plane the unit cell. The antennas are designed to have equal scattering amplitudes and constant phase difference $\Delta\Phi = \pi/4$ between neighbors. **(G)** Finite-difference time-domain (FDTD) simulations of the scattered electric field for the individual antennas composing the array in (F). Plots show the scattered electric field polarized in the x direction for y -polarized plane wave excitation at normal incidence from the silicon substrate. The silicon substrate is located at $z \leq 0$. The antennas are equally spaced at a sub-wavelength separation $\Gamma/8$, where Γ is the unit cell length. The tilted red straight line in (G) is the envelope of the projections of the spherical waves scattered by the antennas onto the x - z plane. On account of Huygens’s



principle, the anomalously refracted beam resulting from the superposition of these spherical waves is then a plane wave that satisfies the generalized Snell’s law (Eq. 2) with a phase gradient $|d\Phi/dx| = 2\pi/\Gamma$ along the interface.

that of an individual straight antenna of length h (Fig. 2B, middle), and therefore the first-order antenna resonance occurs at $h \approx \lambda_{\text{eff}}/2$, where λ_{eff} is the effective wavelength (14). In the anti-symmetric mode, the current distribution in each arm approximates that of one half of a straight antenna of length $2h$ (Fig. 2B, right), and the condition for the first-order resonance of this mode is $2h \approx \lambda_{\text{eff}}/2$.

The polarization of the scattered radiation is the same as that of the incident light when the latter is polarized along \hat{s} or \hat{a} . For an arbitrary incident polarization, both antenna modes are excited but with substantially different amplitude and phase because of their distinctive resonance conditions. As a result, the scattered light can have a polarization different from that of the incident light. These modal properties of the V-antennas allow one to design the amplitude, phase, and polarization state of the scattered light. We chose the incident polarization to be at 45° with respect to \hat{s} and \hat{a} so that both the symmetric and antisymmetric modes can be excited and the scattered light has a substantial component polarized orthogonal to that of the incident light. Experimentally, this allows us to use a polarizer to decouple the scattered light from the excitation.

As a result of the modal properties of the V-antennas and the degrees of freedom in choosing antenna geometry (h and Δ), the cross-polarized scattered light can have a large range of phases and amplitudes for a given wavelength λ_0 ; ana-

lytical calculations of the amplitude and phase response of V-antennas assumed to be made of gold rods are shown in Fig. 2, D and E. In Fig. 2D, the blue and red dashed curves correspond to the resonance peaks of the symmetric and anti-symmetric modes, respectively. We chose four antennas detuned from the resonance peaks, as indicated by circles in Fig. 2, D and E, which provide an incremental phase of $\pi/4$ from left to right for the cross-polarized scattered light. By simply taking the mirror structure (Fig. 2C) of an existing V-antenna (Fig. 2B), one creates a new antenna whose cross-polarized radiation has an additional π phase shift. This is evident by observing that the currents leading to cross-polarized radiation are π out of phase in Fig. 2, B and C. A set of eight antennas were thus created from the initial four antennas, as shown in Fig. 2F. Full-wave simulations confirm that the amplitudes of the cross-polarized radiation scattered by the eight antennas are nearly equal, with phases in $\pi/4$ increments (Fig. 2G).

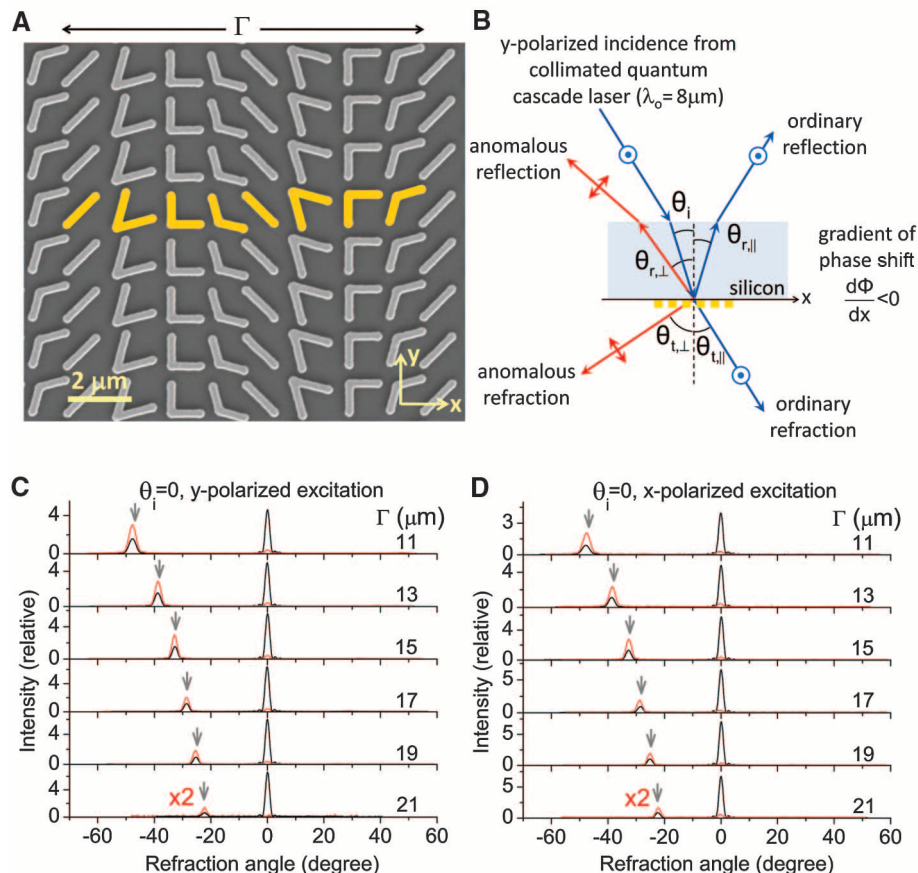
A large phase coverage ($\sim 300^\circ$) can also be achieved by using arrays of straight antennas (fig. S3). However, to obtain the same range of phase shift their scattering amplitudes will be substantially smaller than those of V-antennas (fig. S3). As a consequence of its double resonances, the V-antenna instead allows one to design an array with phase coverage of 2π and equal, yet high, scattering amplitudes for all of the array elements, leading to anomalously reflected and refracted beams of substantially higher intensities.

Experiments on anomalous reflection and refraction. We demonstrated experimentally the generalized laws of reflection and refraction using plasmonic interfaces constructed by periodically arranging the eight constituent antennas as explained in the caption of Fig. 2F. The spacing between the antennas should be subwavelength so as to provide efficient scattering and to prevent the occurrence of grating diffraction. However, it should not be too small; otherwise, the strong near-field coupling between neighboring antennas would perturb the designed scattering amplitudes and phases. A representative sample with the densest packing of antennas, $\Gamma = 11 \mu\text{m}$, is shown in Fig. 3A, where Γ is the lateral period of the antenna array. In the schematic of the experimental setup (Fig. 3B), we assume that the cross-polarized scattered light from the antennas on the left side is phase-delayed as compared with the ones on the right. By substituting into Eq. 2 $-2\pi/\Gamma$ for $d\Phi/dx$ and the refractive indices of silicon and air (n_{Si} and 1) for n_i and n_t , we obtain the angle of refraction for the cross-polarized beam

$$\theta_{t,\perp} = \arcsin[n_{\text{Si}}\sin(\theta_i) - \lambda_0/\Gamma] \quad (6)$$

Figure 3C summarizes the experimental results of the ordinary and the anomalous refraction for six samples with different Γ at normal incidence. The incident polarization is along the y axis in Fig. 3A. The sample with the smallest Γ corresponds to the largest phase gradient and the most

Fig. 3. (A) Scanning electron microscope (SEM) image of a representative antenna array fabricated on a silicon wafer. The unit cell of the plasmonic interface (yellow) comprises eight gold V-antennas of width ~ 220 nm and thickness ~ 50 nm, and it repeats with a periodicity of $\Gamma = 11 \mu\text{m}$ in the x direction and $1.5 \mu\text{m}$ in the y direction. **(B)** Schematic experimental setup for y -polarized excitation (electric field normal to the plane of incidence). **(C and D)** Measured far-field intensity profiles of the refracted beams for y - and x -polarized excitations, respectively. The refraction angle is counted from the normal to the surface. The red and black curves are measured with and without a polarizer, respectively, for six samples with different Γ . The polarizer is used to select the anomalously refracted beams that are cross-polarized with respect to the excitation. The amplitude of the red curves is magnified by a factor of two for clarity. The gray arrows indicate the calculated angles of anomalous refraction according to Eq. 6.



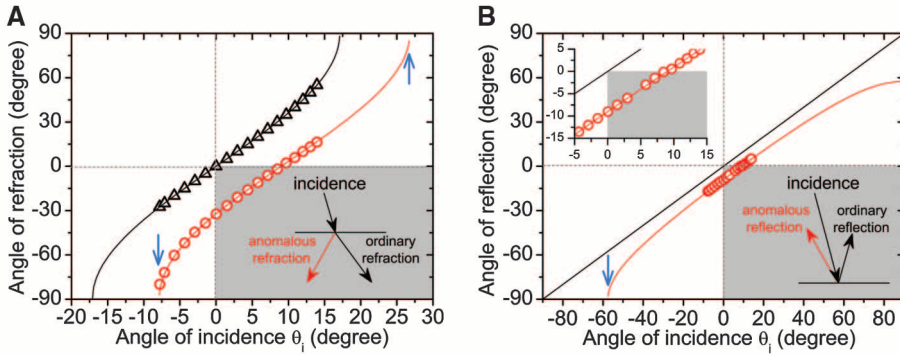
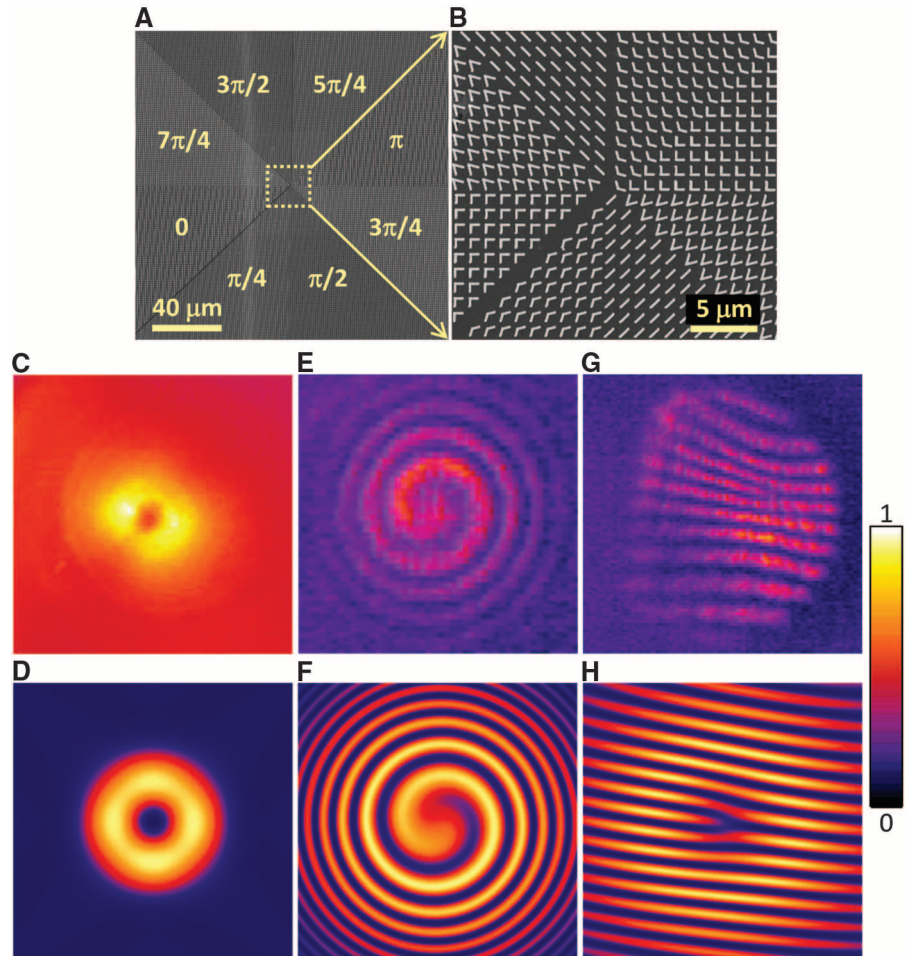


Fig. 4. (A) Angle of refraction versus angle of incidence for the ordinary (black curve and triangles) and anomalous refraction (red curve and dots) for the sample with $\Gamma = 15 \mu\text{m}$. The curves are theoretical calculations made by using the generalized Snell's law for refraction (Eq. 2), and the symbols are experimental data extracted from refraction measurements as a function of the angle of incidence (20). The shaded region represents "negative" refraction for the cross-polarized light, as illustrated in the inset. The blue arrows indicate the modified critical angles for total internal reflection. (B) Angle of reflection versus angle of incidence for the ordinary (black curve) and anomalous (red curve and dots) reflection for the sample with $\Gamma = 15 \mu\text{m}$. The top left inset is the zoom-in view. The curves are theoretical calculations made by using Eq. 4, and the symbols are experimental data extracted from reflection measurements as a function of the angle of incidence (20). The shaded region represents "negative" reflection for the cross-polarized light, as illustrated in the bottom right inset. The blue arrow indicates the critical angle of incidence above which the anomalously reflected beam becomes evanescent. Experiments with lasers emitting at different wavelengths show that the plasmonic interfaces are broadband, anomalously reflecting and refracting light from $\lambda \approx 5 \mu\text{m}$ to $\lambda \approx 10 \mu\text{m}$.

Fig. 5. (A) SEM image of a plasmonic interface that creates an optical vortex. The plasmonic pattern consists of eight regions, each occupied by one constituent antenna of the eight-element set of Fig. 2F. The antennas are arranged so as to generate a phase shift that varies azimuthally from 0 to 2π , thus producing a helicoidal scattered wavefront. (B) Zoom-in view of the center part of (A). (C and D) Respectively, measured and calculated far-field intensity distributions of an optical vortex with topological charge one. The constant background in (C) is due to the thermal radiation. (E and F) Respectively, measured and calculated spiral patterns created by the interference of the vortex beam and a co-propagating Gaussian beam. (G and H) Respectively, measured and calculated interference patterns with a dislocated fringe created by the interference of the vortex beam and a Gaussian beam when the two are tilted with respect to each other. The circular border of the interference pattern in (G) arises from the finite aperture of the beam splitter used to combine the vortex and the Gaussian beams (20). The size of (C) and (D) is 60 mm by 60 mm, and that of (E) to (H) is 30 mm by 30 mm.



efficient light scattering into the cross-polarized beams. We observed that the angles of anomalous refraction agree well with theoretical predictions of Eq. 6 (Fig. 3C). The same peak positions were observed for normal incidence, with polarization along the x axis in Fig. 3A (Fig. 3D). To a good approximation, we expect that the V-antennas were operating independently at the packing density used in experiments (20). The purpose of using a large antenna array ($\sim 230 \mu\text{m}$ by $230 \mu\text{m}$) is solely to accommodate the size of the plane-wave-like excitation (beam radius $\sim 100 \mu\text{m}$). The periodic antenna arrangement is used here for convenience but is not necessary to satisfy the generalized laws of reflection and refraction. It is only necessary that the phase gradient is constant along the plasmonic interface and that the scattering amplitudes of the antennas are all equal. The phase increments between nearest neighbors do not need to be constant, if one relaxes the unnecessary constraint of equal spacing between nearest antennas.

The angles of refraction and reflection are shown in Fig. 4, A and B, respectively, as a function of θ_i for both the silicon-air interface (black curves and symbols) and the plasmonic interface (red curves and symbols) (20). In the range of $\theta_i = 0^\circ$ to 9° , the plasmonic interface

exhibits “negative” refraction and reflection for the cross-polarized scattered light (schematics are shown in the bottom right insets of Fig. 4, A and B). The critical angle for total internal reflection is modified to $\sim -8^\circ$ and $+27^\circ$ (Fig. 4A, blue arrows) for the plasmonic interface in accordance with Eq. 3, compared with $\pm 17^\circ$ for the silicon-air interface; the anomalous reflection does not exist beyond $\theta_i = -57^\circ$ (Fig. 4B, blue arrow).

At normal incidence, the ratio of intensity R between the anomalously and ordinarily refracted beams is ~ 0.32 for the sample with $\Gamma = 15 \mu\text{m}$ (Fig. 3C). R rises for increasing antenna packing densities (Fig. 3, C and D) and increasing angles of incidence [up to $R \approx 0.97$ at $\theta_i = 14^\circ$ (fig. S1B)]. Because of the experimental configuration, we are not able to determine the ratio of intensity between the reflected beams (20), but we expect comparable values.

Vortex beams created by plasmonic interfaces.

To demonstrate the versatility of the concept of interfacial phase discontinuities, we fabricated a plasmonic interface that is able to create a vortex beam (21, 22) upon illumination by normally incident linearly polarized light. A vortex beam has a helicoidal (or “corkscrew-shaped”) equal-phase wavefront. Specifically, the beam has an azimuthal phase dependence $\exp(i\ell\varphi)$ and carries an orbital angular momentum of $L = \ell\hbar$ per photon (23). Here, the topological charge ℓ is an integer, indicating the number of twists of the wavefront within one wavelength; φ is the azimuthal angle with respect to the beam axis; and \hbar is the reduced Planck constant. These peculiar states of light are commonly generated by using a spiral phase plate (24) or a computer-generated hologram (25) and can be used to rotate particles (26) or to encode information in optical communication systems (27).

The plasmonic interface was created by arranging the eight constituent antennas as shown in Fig. 5, A and B. The interface introduces a spiral-like phase shift with respect to the planar wavefront of the incident light, creating a vortex beam with $\ell = 1$. The vortex beam has an annular intensity distribution in the cross section, as viewed in a mid-infrared camera (Fig. 5C); the dark region at the center corresponds to a phase singularity (22). The spiral wavefront of the vortex beam can be revealed by interfering the beam with a co-propagating Gaussian beam (25), producing a spiral interference pattern (Fig. 5E). The latter rotates when the path length of the Gaussian beam was changed continuously relative to that of the vortex beam (movie S1). Alternatively, the topological charge $\ell = 1$ can be identified by a dislocated interference fringe when the vortex and Gaussian beams interfere with a small angle (Fig. 5G) (25). The annular intensity distribution and the interference patterns were well reproduced in simulations (Fig. 5, D, F, and H) by using the calculated amplitude and phase responses of the V-antennas (Fig. 2, D and E).

Concluding remarks. Our plasmonic interfaces, consisting of an array of V-antennas, im-

part abrupt phase shifts in the optical path, thus providing great flexibility in molding of the optical wavefront. This breaks the constraint of standard optical components, which rely on gradual phase accumulation along the optical path to change the wavefront of propagating light. We have derived and experimentally confirmed generalized reflection and refraction laws and studied a series of intriguing anomalous reflection and refraction phenomena that descend from the latter: arbitrary reflection and refraction angles that depend on the phase gradient along the interface, two different critical angles for total internal reflection that depend on the relative direction of the incident light with respect to the phase gradient, and critical angle for the reflected beam to be evanescent. We have also used a plasmonic interface to generate optical vortices that have a helicoidal wavefront and carry orbital angular momentum, thus demonstrating the power of phase discontinuities as a design tool of complex beams. The design strategies presented in this article allow one to tailor in an almost arbitrary way the phase and amplitude of an optical wavefront, which should have major implications for transformation optics and integrated optics. We expect that a variety of novel planar optical components such as phased antenna arrays in the optical domain, planar lenses, polarization converters, perfect absorbers, and spatial phase modulators will emerge from this approach.

Antenna arrays in the microwave and millimeter-wave regions have been used for the shaping of reflected and transmitted beams in the so-called “reflectarrays” and “transmitarrays” (28–31). These typically consist of a double-layer structure comprising a planar array of antennas and a ground plane (in the case of reflectarrays) or another array (in the case of transmitarrays), separated by a dielectric spacer of finite thickness. Reflectarrays and transmitarrays cannot be treated as a single interface for which one can write down the generalized laws because they rely on both antenna resonances and the propagation of waves in the spacer to achieve the desired phase control. The generalization of the laws of reflection and refraction we present is made possible by the deeply subwavelength thickness of our optical antenna arrays and their associated abrupt phase changes, with no contribution from propagation effects. These generalized laws apply to the whole optical spectrum for suitable designer interfaces and can be a guide for the design of new photonic devices.

References and Notes

1. J. B. Pendry, D. Schurig, D. R. Smith, *Science* **312**, 1780 (2006).
2. U. Leonhardt, *Science* **312**, 1777 (2006).
3. W. Cai, V. Shalae, *Optical Metamaterials: Fundamentals and Applications* (Springer, New York, 2009).
4. N. Engheta, R. W. Ziolkowski, *Metamaterials: Physics and Engineering Explorations* (Wiley-IEEE Press, New York, 2006).
5. I. I. Smolyaninov, E. E. Narimanov, *Phys. Rev. Lett.* **105**, 067402 (2010).
6. S. D. Brorson, H. A. Haus, *J. Opt. Soc. Am. B* **5**, 247 (1988).

7. R. P. Feynman, A. R. Hibbs, *Quantum Mechanics and Path Integrals* (McGraw-Hill, New York, 1965).
8. E. Hecht, *Optics* (Addison Wesley, Boston, ed. 3, 1997).
9. H. T. Miyazaki, Y. Kurokawa, *Appl. Phys. Lett.* **89**, 211126 (2006).
10. D. Fattal, J. Li, Z. Peng, M. Fiorentino, R. G. Beausoleil, *Nat. Photonics* **4**, 466 (2010).
11. J. A. Fan *et al.*, *Science* **328**, 1135 (2010).
12. B. Luk'yanchuk *et al.*, *Nat. Mater.* **9**, 707 (2010).
13. R. D. Grober, R. J. Schoelkopf, D. E. Prober, *Appl. Phys. Lett.* **70**, 1354 (1997).
14. L. Novotny, N. van Hulst, *Nat. Photonics* **5**, 83 (2011).
15. Q. Xu *et al.*, *Nano Lett.* **7**, 2800 (2007).
16. M. Sukharev, J. Sung, K. G. Spears, T. Seideman, *Phys. Rev. B* **76**, 184302 (2007).
17. P. Biagioni, J. S. Huang, L. Duò, M. Finazzi, B. Hecht, *Phys. Rev. Lett.* **102**, 256801 (2009).
18. S. Liu *et al.*, *Opt. Lett.* **34**, 1255 (2009).
19. J. Ginn, D. Shelton, P. Krenz, B. Lail, G. Boreman, *Opt. Express* **18**, 4557 (2010).
20. Materials and methods are available as supporting material on Science Online.
21. J. F. Nye, M. V. Berry, *Proc. R. Soc. London A Math. Phys. Sci.* **336**, 165 (1974).
22. M. Padgett, J. Courtial, L. Allen, *Phys. Today* **57**, 35 (2004).
23. L. Allen, M. W. Beijersbergen, R. J. C. Spreeuw, J. P. Woerdman, *Phys. Rev. A* **45**, 8185 (1992).
24. M. W. Beijersbergen, R. P. C. Coerwinkel, M. Kristensen, J. P. Woerdman, *Opt. Commun.* **112**, 321 (1994).
25. N. R. Heckenberg, R. McDuff, C. P. Smith, A. G. White, *Opt. Lett.* **17**, 221 (1992).
26. H. He, M. E. J. Friese, N. R. Heckenberg, H. Rubinsztein-Dunlop, *Phys. Rev. Lett.* **75**, 826 (1995).
27. G. Gibson *et al.*, *Opt. Express* **12**, 5448 (2004).
28. D. M. Pozar, S. D. Targonski, H. D. Syrigos, *IEEE Trans. Antenn. Propag.* **45**, 287 (1997).
29. J. A. Encinar, *IEEE Trans. Antenn. Propag.* **49**, 1403 (2001).
30. C. G. M. Ryan *et al.*, *IEEE Trans. Antenn. Propag.* **58**, 1486 (2010).
31. P. Padilla, A. Muñoz-Acevedo, M. Sierra-Castañer, M. Sierra-Pérez, *IEEE Trans. Antenn. Propag.* **58**, 2571 (2010).

Acknowledgments: The authors acknowledge helpful discussion with J. Lin, R. Blanchard, and A. Belyanin. The authors acknowledge support from the National Science Foundation (NSF), Harvard Nanoscale Science and Engineering Center (NSEC) under contract NSF/PHY 06-46094, and the Center for Nanoscale Systems (CNS) at Harvard University. This work was supported in part by the Defense Advanced Research Projects Agency (DARPA) N/MEMS S&T Fundamentals program under grant N66001-10-1-4008 issued by the Space and Naval Warfare Systems Center Pacific (SPAWAR). Z.G. acknowledges funding from the European Communities Seventh Framework Programme (FP7/2007-2013) under grant agreement P10F-GA-2009-235860. M.A.K. is supported by NSF through a Graduate Research Fellowship. Harvard CNS is a member of the National Nanotechnology Infrastructure Network. The Lumerical (Vancouver, BC, Canada) FDTD simulations in this Research Article were run on the Odyssey cluster supported by the Harvard Faculty of Arts and Sciences Sciences Division Research Computing Group.

Supporting Online Material

www.sciencemag.org/cgi/content/full/science.1210713/DC1
Materials and Methods
SOM Text
Figs. S1 to S6
References (32–39)
Movie S1

5 July 2011; accepted 19 August 2011
Published online 1 September 2011;
10.1126/science.1210713



www.sciencemag.org/cgi/content/full/science.1210713/DC1

Supporting Online Material for

Light Propagation with Phase Discontinuities: Generalized Laws of Reflection and Refraction

Nanfang Yu, Patrice Genevet, Mikhail A. Kats, Francesco Aieta, Jean-Philippe Tetienne, Federico Capasso, Zeno Gaburro

Published 1 September 2011 on *Science Express*

DOI: 10.1126/science.1210713

This PDF file includes:

Materials and Methods

SOM Text

Figs. S1 to S6

References (32–39)

Other Supporting Online Material for this manuscript includes the following:

(available at www.sciencemag.org/cgi/content/full/science.1210713/DC1)

Movie S1

Materials and Methods

Gold V-antenna arrays, $230\ \mu\text{m} \times 230\ \mu\text{m}$ in size, were fabricated using electron-beam lithography on $280\text{-}\mu\text{m}$ thick intrinsic silicon wafers. The thickness of gold is $50\ \text{nm}$ and 10-nm titanium is used as the adhesion layer. The width of the antenna arms is $\sim 220\ \text{nm}$. The skin depth of gold (i.e., $1/e$ decay distance of the magnitude of electric field inside the metal) is $\sim 25\ \text{nm}$ at our operating wavelength $\lambda_0 \approx 8\ \mu\text{m}$. The arrays were surrounded by opaque gold masks. Note that there is native SiO_2 of a couple of nanometers on our silicon wafers, and the oxidation has a strong but narrow lattice absorption band centered at $\lambda_0 \approx 9\ \mu\text{m}$ (32). The experiments were not significantly affected because our operating wavelength was on the wings of this absorption band.

To demonstrate the generalized laws of reflection and refraction, antenna arrays with different packing densities were fabricated: the eight-antenna unit cell repeats in the horizontal direction with a periodicity of $\Gamma = 11, 13, 15, 17, 19,$ or $21\ \mu\text{m}$, and in the vertical direction with a periodicity of $1.5\ \mu\text{m}$ (one representative sample with $\Gamma = 11\ \mu\text{m}$ is shown in Fig. 3A). The plasmonic interface for creating optical vortices consists of a square lattice of antennas with a lattice constant of $1.5\ \mu\text{m}$ (Figs. 5A and B).

A buried-heterostructure quantum cascade laser (QCL) with central wavelength $8\ \mu\text{m}$ and spectral width $\sim 0.2\ \mu\text{m}$ was used as the light source in the experiments for demonstrating the generalized laws of reflection and refraction. The QCL was operated in pulsed mode with $1.5\text{-}\mu\text{s}$ pulse width and 80-kHz repetition rate at room temperature and the average output power is about $5\ \text{mW}$. A one-inch diameter zinc selenide (ZnSe) lens with one-inch focal length was used to collimate the emission from the QCL and another one-inch diameter ZnSe lens with 20-inch focal length was used to focus the laser beam on the antenna array. The beam radius w_0 on the sample is $\sim 100\ \mu\text{m}$ (w_0 is the radius at which the field amplitude drops to $1/e$ of the peak value), and the Rayleigh length of the Gaussian beam is $\sim 4\ \text{mm}$. This ensures that the whole antenna array is illuminated by a plane-wave-like excitation. The laser beam was incident from the back side of the silicon wafer, which was not decorated with antennas. Because of the gold masks surrounding the arrays, the fraction of the incident beam that is not impinging on the array was completely reflected. The sample was mounted at the center of a motorized rotation stage, and a liquid-nitrogen-cooled mercury-cadmium-telluride (MCT) detector $\sim 15\ \text{cm}$ away was angularly scanned to measure the far-field intensity profiles. Our measurements were performed with a resolution of 0.2 degrees. A polarizer was added between the sample and the detector to isolate antenna radiation cross-polarized with respect to the incident light.

The experimental setup for creating and characterizing the vortex beams was based on the above setup except for the following changes. A distributed-feedback continuous-wave QCL emitting monochromatic light at $\lambda_0 = 7.75\ \mu\text{m}$ with average output power a few mW was used as the light source. The buried heterostructure QCL used in the previous experiment has multiple longitudinal modes, which blur interference fringes, making vortex characterization impossible. A beam splitter was placed in the path of the

incident beam, between the lens with 20-inch focal length and the sample. The transmitted light from the splitter impinged on the vortex sample (Fig. 5A), while the reflected light was flipped in polarization by 90 degrees and beam-expanded to serve as a reference beam. After passing through the sample, the output in crossed polarization was isolated by the polarizer and was then allowed to interfere with the reference beam. A mid-infrared camera was used to record the interference fringes.

SOM Text

Dipolar resonances of optical antennas

The amplitude and phase response of the rod antenna presented in Fig. 2A is calculated by analytically solving Hallén's integral equations for linear antennas (33). The antenna is located in vacuum and has a variable length L and a circular cross-section with radius $a = L/50$. Incident monochromatic light impinges normal to the axis of the rod and is polarized along it. The scattered light is monitored in the far-field along the direction of the incident light. The phase of the scattered light is defined relative to that of the excitation.

The phase response versus the length of a straight rod antenna can be understood qualitatively in the following way. First, for an optically small antenna ($L/\lambda_0 \ll 1$), the charges in the antenna instantaneously follows the incident field, $\tilde{q} \propto \tilde{E}_{inc} = E_{inc} \exp(i\omega t)$, where \tilde{q} is the accumulated charges at one end of the antenna. Therefore, the emitted light, which is proportional to the acceleration of the charges (Larmor formula (34)), is $\tilde{E}_{scat} \propto \partial^2 \tilde{q} / \partial t^2 \propto -\omega^2 \tilde{E}_{inc}$. That is, the incident and scattered light are π out of phase. At the first-order antenna resonance ($L/\lambda_0 \sim 1/2$), the incident field is in phase with the current at the center of the antenna $\tilde{I} \propto \tilde{E}_{inc}$ and therefore drives the current most efficiently. As a result, $\tilde{E}_{scat} \propto \partial^2 \tilde{q} / \partial t^2 \propto \partial \tilde{I} / \partial t \propto i\omega \tilde{E}_{inc}$: the phase difference between \tilde{E}_{scat} and \tilde{E}_{inc} is $\pi/2$. For a long antenna with length comparable to the wavelength ($L/\lambda_0 \sim 1$), the antenna impedance (defined as the incident field divided by the current at the center of the antenna) is primarily inductive, $\tilde{I} \propto -i\tilde{E}_{inc}$. Therefore, the scattered and incident light are almost in phase, $\tilde{E}_{scat} \propto \partial \tilde{I} / \partial t \propto \tilde{E}_{inc}$.

In summary, at a fixed excitation wavelength, the antenna impedance changes from capacitive, to resistive, and to inductive cross a resonance as the antenna length increases. A single antenna resonance is therefore only able to provide a range of phase change at most π between the scattered and incident light without resorting to mirror structures as demonstrated in Figs. 2B and C.

The phase coverage of a straight rod antenna cannot be extended beyond π by using higher-order antenna resonances. Figure S2 shows the first three resonances of a straight rod antenna calculated by solving Hallén's integral equations (33). The phase of the scattered light changes within a range of π (Fig. S2A) and the phase shifts at all antenna

resonances are $\sim\pi/2$ (Fig. S2A, zoom-in views). These phenomena can be understood by studying the instantaneous current distributions at antenna resonances. In Fig. S2B positive (negative) value of current means that the current flow is in the same (opposite) direction with respect to that of the instantaneous incident electric field. The number of positive lobes in any current distribution is larger than that of negative lobes by one (for example, three versus two for the third-order antenna resonance). Therefore, at resonances, the far-field radiation monitored in the broadside direction (perpendicular to the antenna axis) is contributed primarily by one positive current lobe (radiations generated by a pair of lobes with opposite signs interfere destructively) and will have the same phase. Indeed, in theory, for an infinitely-thin antenna made of perfect electric conductors, the phase shift between the scattered and incident light will always be $\pi/2$ at resonances (33). It is not exactly $\pi/2$ in our calculations because of the finite antenna radius.

Figure S2C shows the far-field radiation profiles for the first three antenna resonances. Antennas at higher-order resonances support current standing waves with multiple lobes, leading to complicated radiation patterns with a non-uniform spatial phase distribution. They are therefore undesirable for the construction of plasmonic interfaces. Antennas operating at the first-order resonance instead produce spherical wavefronts (33): the phase of radiation is constant over the wavefront and the main lobe of the radiation is broad (Fig. S2C). In our experiments the V-antennas were designed to operate in the vicinity of the first-order resonance for both the symmetric and antisymmetric modes (Fig. 2D).

Plasmonic interface consisting of straight antennas

A plasmonic interface conceptually simpler than the one presented in the main text could be constructed using arrays of straight rod antennas. The phase and amplitude of the cross-polarized radiation could be controlled by the length and orientation of the rods (Fig. S3). However, the phase shift cannot cover the complete 2π range while maintaining large scattering amplitudes in this case.

Figures S3A and B show, respectively, the amplitude and phase shift of cross-polarized radiation from a straight rod antenna as a function of its length and orientation. When the rod is aligned with the incident polarization, the largest antenna current is excited but no light is scattered into the orthogonal polarization direction; when the rod is perpendicular to the incident polarization, no antenna current is excited. Therefore, the amplitude of the cross-polarized scattered light vanishes for $\Theta = 0, 90,$ and 180 degrees in Fig. S3A; Θ is the angle between the rod axis and the incident polarization. The scattering of light into the cross-polarization is most efficient when $\Theta = 45$ or 135 degrees. The phases of antenna radiation differ by π for mirror-symmetric antennas with orientation angles Θ and $180 - \Theta$ degrees, respectively (the left and right halves of Fig. S3B).

To reconstruct plane waves from the cross-polarized scattered waves from an antenna array, the scattering amplitude of the array elements must be constant. This

constraint defines a family of equal-value contours in the amplitude response as a two dimensional function of the antenna's parameters L and Θ . One such contour is shown as the dashed curve in Fig. S3A. The curve represents the loci of mutually compatible parameters L and Θ , in terms of the same amplitude response. The transfer of each contour to the phase response diagram shows the available phase range for that specific amplitude. For the previous example, the dashed curve in Fig. S3B indicates that the available phase coverage is only about 110 degrees, from -30 degrees to -140 degrees, for a scattering amplitude about half of the maximum value. This phase range can be doubled to about 220 degrees with mirror-symmetric antennas. The phase coverage can potentially reach ~ 325 degrees (according to the color map of Fig. S3B) for rod antennas but the corresponding scattering amplitude will be very small. As a consequence of its double resonances, the V-antenna discussed in the main text instead allows one to design an array with phase coverage of 2π and large scattering amplitudes ($\sim 75\%$ of the maximum, according to Fig. 2D) for all of the array elements.

Scattering and absorption cross-sections of V-antennas

The simulated scattering and absorption cross-sections for the four constituent antennas (Figs. 2D and E) are shown in Fig. S4. These were calculated based on finite-different time-domain simulations using realistic materials properties (35). The simulation results indicate that at $\lambda_o = 8 \mu\text{m}$ the scattering cross-sections σ_{scat} of the antennas range from 0.7 to $2.5 \mu\text{m}^2$, which are comparable to or smaller than the average area each antenna occupies, σ_{aver} (i.e., the total area of the array divided by the number of antennas). For example, σ_{aver} is $\sim 2.06 \mu\text{m}^2$ for the sample with the densest packing corresponding to $\Gamma = 11 \mu\text{m}$ (Fig. 3A). Therefore, it is reasonable to assume that near-field coupling between antennas will introduce only small deviations from the response of isolated antennas. Figure S4 also shows that the absorption cross-sections σ_{abs} are $\sim 5-7$ times smaller than σ_{scat} , indicating comparatively small Ohmic losses in the antennas.

Analytical model for V-antennas

The optical properties of V-antennas are calculated by solving the integral equations for the currents of the symmetric and antisymmetric antenna modes. Once the current distributions are known, the far-field radiation of V-antennas can be readily calculated. Note that the complete derivation is lengthy and we only describe the framework of our model, which includes:

1. The integral equations and boundary conditions for the symmetric and antisymmetric antenna modes, and
2. The analytical solutions to the equations based on an iteration method.

We assume that the V-antennas are made of gold rods with a circular cross-section with radius a embedded in a homogenous dielectric material with refractive index n_{eff} (Fig. S5). Such geometry is chosen for the convenience of analytical derivation. We choose appropriate a and n_{eff} to make sure a proper modeling of the V-antennas used in

experiments, which were fabricated on silicon substrates and have a rectangular cross-section.

1. The antenna radius a was chosen to be 100 nm. Simulations show that gold rod antennas with such dimensions have very similar optical responses, in terms of the positions and the widths of the resonance peaks, compared to gold antennas with a rectangular cross-section of 220 nm \times 50 nm (all other geometry and simulation conditions kept the same).

2. The effective refractive index n_{eff} was chosen to be 2.6. Simulations of straight rectangular antennas placed on a silicon substrate were conducted and n_{eff} was extracted by using an empirical formula for the first-order antenna resonance (36): $\lambda_{\text{res}} \approx 2.1(L+w)n_{\text{eff}}$, where λ_{res} is the resonance wavelength, L and w are, respectively, the antenna length and width. The extracted value is close to theoretical estimation of n_{eff} (36): $n_{\text{eff}} \approx [(n_{\text{air}}^2 + n_{\text{Si}}^2)/2]^{1/2} = 2.52$, where $n_{\text{Si}} = 3.4$ is the refractive index of silicon at $\lambda_0 = 8 \mu\text{m}$.

In our theoretical model, the V-antenna is located in the z-x plane (Fig. S5). The two antenna rods, denoted No. 1 and No. 2, are aligned with z- and s-axis, respectively. The wavevector of the linearly polarized incident light, $\vec{\beta}$, lies in the symmetry plane of the V-antenna (light blue in Fig. S5A) and the angle between $\vec{\beta}$ and the z-x plane is θ .

The antenna response can be decomposed into a linear combination of two modes characterized by symmetric and antisymmetric current distributions as discussed in the main text. For the antisymmetric mode, the currents in the two rods satisfy:

$$I_{1z}^a(z) = -I_{2s}^a(s) \quad \text{for } z = s \quad (\text{s1})$$

while for the symmetric mode:

$$I_{1z}^s(z) = I_{2s}^s(s) \quad \text{for } z = s \quad (\text{s2})$$

where we have used superscripts “a” and “s” to distinguish the two modes.

The boundary condition on the surface of the rod No. 1 reads:

$$E_{1z} = -\frac{\partial \phi_1}{\partial z} - j\omega A_{1z} = -\frac{j\omega}{\beta^2} \left(\frac{\partial}{\partial z} \nabla \cdot \vec{A}_1 + \beta^2 A_{1z} \right) = 0 \quad (\text{s3})$$

where \vec{A}_1 and ϕ_1 are the vector and scalar potentials on the surface of the rod No. 1, respectively, A_{1z} is the z-component of \vec{A}_1 , β is wavevector, and ω is angular

frequency. Note that we have used the Lorentz gauge $\nabla \cdot \vec{A}_1 = -j \frac{\beta^2}{\omega} \phi_1$. Equation (s3)

states that the tangential component of the electric field on the surface of the rod E_{1z} is zero, which is only valid for antennas made of perfect electric conductors. It can be generalized to account for realistic metals, which will be discussed at the end of this section.

There are two additional boundary conditions at the ends and joint of the V-antenna. For the antisymmetric mode, we have:

$$I_{1z}^a(z=h) = I_{2s}^a(s=h) = 0 \quad (\text{s4})$$

$$\phi_1^a(z=0) = \phi_2^a(s=0) = 0 \quad (\text{s5})$$

The latter is due to antisymmetry: the scalar potentials of the two rods must have opposite signs and the same magnitude for the antisymmetric mode, $\phi_1^a(z) = -\phi_2^a(s)$; meanwhile, due to electrical contact of the two rods at the joint, we should have $\phi_1^a(z=0) = \phi_2^a(s=0)$. As a result, the scalar potentials at the joint can only be zero.

For the symmetric mode, we have:

$$I_{1z}^s(z=h) = I_{2s}^s(s=h) = 0 \quad (\text{s6})$$

$$A_{1z}^s(z=0) = A_{2s}^s(s=0) \approx 0 \quad (\text{s7})$$

The vector potentials at the joint are nearly zero because they are primarily determined by the currents in the immediate vicinity of the joint (Eqs. (s9)-(s11)), which are nearly zero for the symmetric mode. For a better approximation, one can calculate $A_{1z}^s(z=0)$ assuming that the current distribution in the rods is the same as that of an isolated straight rod antenna of length h and use the result to replace the zero at the right-hand side of (s7).

There are three contributions to the vector potential on an antenna rod: that due to the current distribution of the antenna rod (“self interaction”), that due to the current distribution of the other antenna rod (“mutual interaction”), and that due to the incident light. For example, $A_{1z}^a = A_{11z}^a + A_{12z}^a + A_{13z}^a$ is the vector potential on the surface of the first antenna rod for the antisymmetric mode, where the three terms on the right-hand side represent the three contributions, respectively. As a result, Eq. (s3) can be rewritten as

$$\left[\frac{\partial^2 (A_{11z}^a + A_{12z}^a)}{\partial z^2} + \beta^2 (A_{11z}^a + A_{12z}^a) \right] + \frac{\partial^2 A_{12x}^a}{\partial z \partial x} + \left(\frac{\partial}{\partial z} \nabla \cdot \vec{A}_{13}^a + \beta^2 A_{13z}^a \right) = 0 \quad (\text{s8})$$

where

$$A_{11z}^a = \frac{\mu_o}{4\pi} \int_0^h I_{1z}^a(z') \exp[-j\beta R_1(z, z')] / R_1(z, z') dz' \quad (\text{s9})$$

$$A_{12z}^a = \cos(\Delta) \frac{\mu_o}{4\pi} \int_0^h I_{2s}^a(s') \exp[-j\beta R_{12}(z, s')] / R_{12}(z, s') ds' \quad (\text{s10})$$

$$= -\cos(\Delta) \frac{\mu_o}{4\pi} \int_0^h I_{1z}^a(z') \exp[-j\beta R_{12}(z, z')] / R_{12}(z, z') dz'$$

$$A_{12x}^a = -\sin(\Delta) \frac{\mu_o}{4\pi} \int_0^h I_{1z}^a(z') \exp[-j\beta R_{12}(z, z')] / R_{12}(z, z') dz' \quad (\text{s11})$$

are, respectively, contributions to the vector potential on the rod No. 1 from its own current, and from the z- and x-component of the current in the rod No. 2.

$R_1(z, z') = \sqrt{(z-z')^2 + a^2}$ and $R_{12}(z, s') = \sqrt{z^2 - 2zs' \cos(\Delta) + s'^2 + a^2}$ are, respectively, the distances between the element of integration on the two rods (primed coordinates) and the monitor point on the rod No. 1 (Fig. S5B). μ_o is the magnetic permeability of the surrounding dielectric. Note that in (s10) and (s11), we have used the antisymmetric condition (s1).

The contribution to the vector potential on the rod No. 1 from the incident light satisfies the following equation (33):

$$\frac{\partial}{\partial z} \nabla \cdot \vec{A}_{13}^a + \beta^2 A_{13z}^a = \frac{j\beta^3}{\omega} \left(1 - \frac{q^2}{\beta^2}\right) U_{inc}^a \exp(jqz) \quad (s12)$$

in which

$$q = \beta \cos(\theta) \cos(\Delta/2) \quad (s13)$$

and

$$U_{inc}^a = \frac{E_{inc}^a \sin(\Delta/2)}{\beta \left[\sin^2(\theta) + \cos^2(\theta) \sin^2(\Delta/2) \right]} \quad (s14)$$

where E_{inc}^a is the component of the incident electric field that drives the antisymmetric mode (Fig. S5A).

Using (s8) and boundary condition (s5), we can derive the integral equation for the current in the rod No. 1 for the antisymmetric mode:

$$\int_0^h I_{1z}^a(z') K^a(z, z') dz' = \frac{-4\pi j}{\eta_o} \left[C_1 \cos(\beta z) - \frac{jq}{\beta} U_{inc}^a \sin(\beta z) \right] + J^a(z) - \frac{4\pi j}{\eta_o} U_{inc}^a \exp(jqz) \quad (s15)$$

where

$$K^a(z, z') = \exp[-j\beta R_1(z, z')] / R_1(z, z') - \cos(\Delta) \exp[-j\beta R_{12}(z, z')] / R_{12}(z, z') \quad (s16)$$

$$J^a(z) = \sin^2(\Delta) \int_0^z \left\{ \int_0^h I_{1z}^a(z') [1 + j\beta R_{12}(w, z')] \exp[-j\beta R_{12}(w, z')] / R_{12}^3(w, z') z' dz' \right\} \cos[\beta(z-w)] dw \quad (s17)$$

η_o is the impedance of the surrounding medium, and C_1 in (s15) is a constant to be determined.

We then follow an iteration procedure as discussed in Ref. (33) and use boundary condition (s4) to eliminate C_1 and solve the integral equation (s15). The current distribution in the rod No.1 for the antisymmetric mode to the n^{th} -order correction is:

$$I_{1z}^a(z) = \frac{-4\pi j}{\eta_o \psi^a} \frac{jq U_{inc}^a \left[\sum_{m=0}^n G_m^a(h) / \psi^{am} \sum_{m=0}^n F_m^a / \psi^{am} - \sum_{m=0}^n G_{mz}^a / \psi^{am} \sum_{m=0}^n F_m^a(h) / \psi^{am} \right]}{\sum_{m=0}^n F_m^a(h) / \psi^{am}} + U_{inc}^a \left[\sum_{m=0}^n H_{mz}^a / \psi^{am} \sum_{m=0}^n F_m^a(h) / \psi^{am} - \sum_{m=0}^n H_m^a(h) / \psi^{am} \sum_{m=0}^n F_{mz}^a / \psi^{am} \right] \quad (s18)$$

in which

$$\psi^a = \left| \int_0^h \frac{\cos(\beta z') - \cos(\beta h)}{\cos(\beta z) - \cos(\beta h)} K^a(z, z') dz' \right| \quad (s19)$$

$$F_{mz}^a = F_m^a(z) - F_m^a(h), G_{mz}^a = G_m^a(z) - G_m^a(h), H_{mz}^a = H_m^a(z) - H_m^a(h) \quad (\text{s20})$$

$$F_0^a(z) = \cos(\beta z), G_0^a(z) = \sin(\beta z), H_0^a(z) = \exp(jqz) \quad (\text{s21})$$

and

$$X_m^a(z) = X_{m-1,z}^a \psi^a - \int_0^h X_{m-1,z'}^a K^a(z, z') dz' + J^a(I_{1z}^a(z') = X_{m-1,z'}^a, z) \quad \text{for } m \geq 1 \quad (\text{s22})$$

where X can be F , G , or H , and $J^a(I_{1z}^a(z') = X_{m-1,z'}^a, z)$ is the same as $J^a(z)$ in (s17) but with $X_{m-1,z'}^a$ substituted for $I_{1z}^a(z')$.

According to (s18), the solution with the first-order correction is:

$$I_{1z,1st}^a(z) = \frac{-4\pi j}{\eta_o \psi^a} \frac{-U_{inc}^a [\exp(jqh) \cos(\beta z) - \exp(jqz) \cos(\beta h)] + \frac{jq}{\beta} U_{inc}^a \sin[\beta(h-z)] + M_1^a(z) / \psi^a}{\cos(\beta h) + A_1^a / \psi^a} \quad (\text{s23})$$

where

$$M_1^a(z) = U_{inc}^a [H_{0z}^a F_1^a(h) + H_{1z}^a F_0(h) - H_0(h) F_{1z}^a - H_1^a(h) F_{0z}^a] + \frac{jq}{\beta} U_{inc}^a [G_0(h) F_{1z}^a + G_1^a(h) F_{0z}^a - G_{0z}^a F_1^a(h) - G_{1z}^a F_0(h)] \quad (\text{s24})$$

and

$$A_1^a = F_1^a(h) \quad (\text{s25})$$

The zeroth-order current for normal incidence ($q=0$) is

$$I_{1z,0,normal}^a(z) = \frac{4\pi j U_{inc}^a}{\eta_o \psi^a} \frac{\cos(\beta z) - \cos(\beta h)}{\cos(\beta h)} \quad (\text{s26})$$

which is exactly the same as the zeroth-order solution of the current in an infinitely-thin *straight* receiving antenna of length $2h$ (33). This makes sense because in the zeroth-order approximation the electromagnetic interactions between different parts of a V-antenna are not considered. Therefore its optical response is only determined by the antenna length as shown in (s26).

We can similarly derive the integral equation for the current in the rod No. 1 for the symmetric mode:

$$\int_0^h I_{1z}^s(z') K^s(z, z') dz' = \frac{-4\pi j}{\eta_o} [-U_{inc}^s \cos(\beta z) + C_2 \sin(\beta z)] + J^s(z) - \frac{4\pi j}{\eta_o} U_{inc}^s \exp(jqz) \quad (\text{s27})$$

where

$$K^s(z, z') = \exp[-j\beta R_1(z, z')] / R_1(z, z') + \cos(\Delta) \exp[-j\beta R_{12}(z, z')] / R_{12}(z, z') \quad (\text{s28})$$

$$J^s(z) = \frac{4\pi j}{\eta_o} \left\{ \beta \int_0^z \xi_x^s(w) \cos[\beta(z-w)] dw - \sin(\beta z) \xi_x^s(z=0) \right\} \quad (\text{s29})$$

$$\xi_x^s(z) = \sin^2(\Delta) \frac{j\omega\mu_o}{4\pi\beta^2} \int_0^h I_{1z}^s(z') [1 + j\beta R_{12}(z, z')] \exp[-j\beta R_{12}(z, z')] / R_{12}^3(z, z') z' dz' \quad (s30)$$

$$U_{inc}^s = \frac{E_{inc}^s \sin(\theta) \cos(\Delta/2)}{\beta [\sin^2(\theta) + \cos^2(\theta) \sin^2(\Delta/2)]} \quad (s31)$$

in which E_{inc}^s is the component of the incident electric field that drives the symmetric mode (Fig. S5A).

The current distribution in the rod No.1 for the symmetric mode to the n^{th} -order correction is

$$I_{1z}^s(z) = \frac{-4\pi j}{\eta_o \psi^s} \frac{U_{inc}^s \left[\sum_{m=0}^n F_m^s(h) / \psi^{sm} \sum_{m=0}^n G_{mz}^s / \psi^{sm} - \sum_{m=0}^n F_{mz}^s / \psi^{sm} \sum_{m=0}^n G_m^s(h) / \psi^{sm} \right] + U_{inc}^s \left[\sum_{m=0}^n H_{mz}^s / \psi^{sm} \sum_{m=0}^n G_m^s(h) / \psi^{sm} - \sum_{m=0}^n H_m^s(h) / \psi^{sm} \sum_{m=0}^n G_{mz}^s / \psi^{sm} \right]}{\sum_{m=0}^n G_m^s(h) / \psi^{sm}} \quad (s32)$$

where

$$\psi^s = \left| \int_0^h \frac{\sin[\beta(h-z')] - [\sin(\beta z') - \sin(\beta h)]}{\sin[\beta(h-z)] - [\sin(\beta z) - \sin(\beta h)]} K^s(z, z') dz' \right| \quad (s33)$$

and F , G , and H are similarly defined as in (s20)-(s22).

The current distribution with the first-order correction is:

$$I_{1z,1st}^s(z) = \frac{-4\pi j}{\eta_o \psi^s} \frac{-U_{inc}^s \sin[\beta(h-z)] - U_{inc}^s [\exp(jqh) \sin(\beta z) - \exp(jqz) \sin(\beta h)] + M_1^s(z) / \psi^s}{\sin(\beta h) + A_1^s / \psi^s} \quad (s34)$$

where

$$M_1^s(z) = U_{inc}^s [F_0(h)G_{1z}^s + F_1^s(h)G_{0z}^s - F_{0z}^s G_1^s(h) - F_{1z}^s G_0(h)] + U_{inc}^s [H_{0z}^s G_1^s(h) + H_{1z}^s G_0(h) - H_0(h)G_{1z}^s - H_1^s(h)G_{0z}^s] \quad (s35)$$

and

$$A_1^s = G_1^s(h) \quad (s36)$$

The zeroth-order current for normal incidence ($q = 0$) is

$$I_{1z,0,normal}^s(z) = \frac{4\pi j U_{inc}^s \sin[\beta(h-z)] + [\sin(\beta z) - \sin(\beta h)]}{\eta_o \psi^s \sin(\beta h)} \quad (s37)$$

Let $h = 2h'$ and $z = z' + h'$ in (s37), we have

$$I_{1z,0,normal}^s(z) \Big|_{\substack{h=2h' \\ z=z'+h'}} = \frac{4\pi j U_{inc}^s \cos(\beta z') - \cos(\beta h')}{\eta_o \psi^s \cos(\beta h')} \quad (s38)$$

Thus we recover the zeroth-order current distribution in an infinitely-thin *straight* receiving antenna of length $2h' = h$. One can further check that according to (s37):

$$I_{1z,0}^s(z=0) = 0, \quad (s39)$$

That is, there is no current at the joint of the V-antenna for the symmetric mode.

The above derivation assumes that the antenna is made of perfect electric conductors. To model real metals, one has to add a term to the right-hand side of (s3) and the new boundary condition on the surface of the rod No. 1 reads:

$$E_{1z} = -\frac{j\omega}{\beta^2} \left(\frac{\partial}{\partial z} \nabla \cdot \bar{A}_1 + \beta^2 A_{1z} \right) = z^i I_z \quad (s40)$$

where z^i is the surface impedance per unit length of the antenna (33):

$$z^i = \frac{\eta_m}{2\pi a} = \frac{1}{2\pi a} \sqrt{\frac{\mu}{\epsilon_r - j\sigma/\omega}} \quad (s41)$$

The concept of surface impedance is valid for mid-infrared and longer wavelengths (37). If the displacement current is much smaller than the conduction current as in the case of highly conductive metals ($\omega\epsilon_r \ll \sigma$) the impedance per unit length of antenna will be

$$z^i \approx \frac{1+j}{2\pi a} \sqrt{\frac{\omega\mu}{2\sigma}} \quad (s42)$$

As a result of the correction in (s40), one additional term should be added to (s22) for the antisymmetric mode and the similar expression for the symmetric mode (other equations previously derived will not change):

$$X_m(z) = \frac{j4\pi z^i}{\eta_o} \int_0^z X_{m-1,s} \sin[\beta(z-s)] ds + X_{m-1,z} \psi - \int_0^h X_{m-1,z'} K(z, z') dz' + J(I_{1z}(z') = X_{m-1,z'}, z) \quad (s43)$$

Combining the results of current distributions for the antisymmetric and symmetric modes, (s18) and (s32), the currents in the two antenna rods can be written as

$$I_1(z) = I_{1z}^a(z) + I_{1z}^s(z) \quad (s44)$$

$$I_2(s) = -I_{1z}^a(s) + I_{1z}^s(s) \quad (s45)$$

based on which one can calculate the amplitude and phase shift of antenna radiation in the far-field. Corrections up to the second order were used in our calculations (Figs. 2D and E in the main text).

Effects of the silicon slab

For an antenna array located on the interface between two semi-infinite spaces, air and silicon, the ratio of power emitted into the two spaces should be, in theory, equal to the ratio between their refractive indices (38, 39) (Fig. S6):

$$\frac{a}{b} = \frac{n_{air}}{n_{Si}} \quad (s46)$$

which is about 1/3.4 at $\lambda_0 = 8 \mu\text{m}$. This ratio will be modified for a silicon slab of finite thickness, which functions as a Fabry-Pérot resonator for the light radiated into the slab (Fig. S6). The power reflection coefficient at the bottom silicon-air interface is R_1 , while that at the top interface decorated with plasmonic antennas is R_2 . Keeping in mind that the spectral width of our laser source is larger than the Fabry-Pérot free spectral range by one order of magnitude, we sum the power instead of the amplitude of the antenna radiations exiting from the upper and lower surface of the silicon slab (Fig. S6) and obtain:

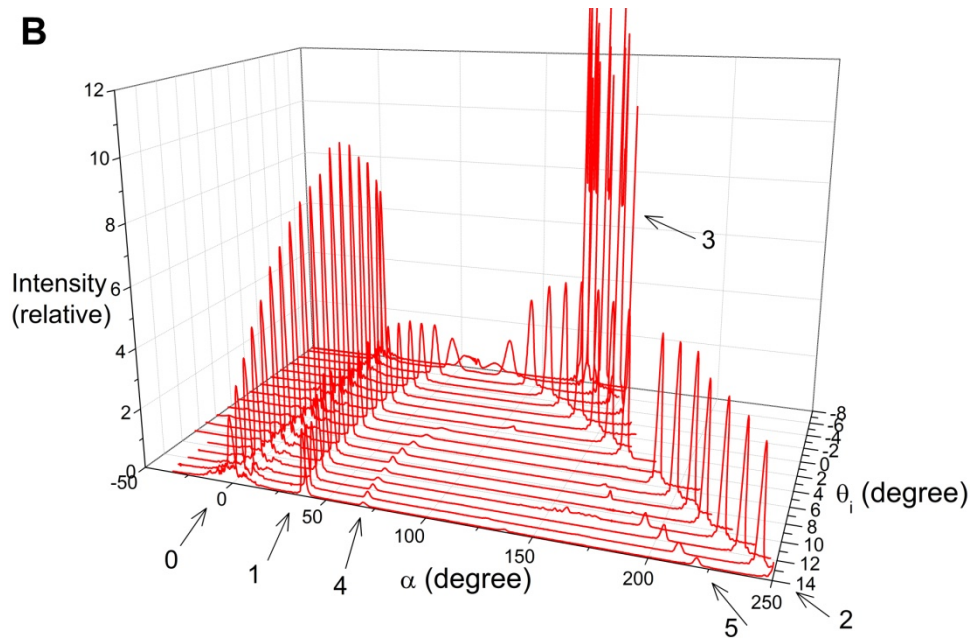
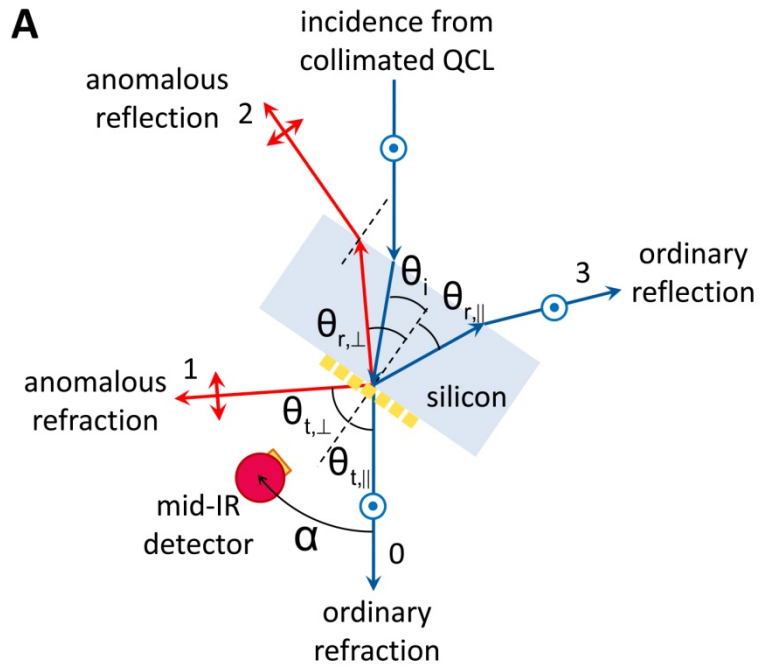
$$I_{tran,\perp} = a + \frac{bR_1(1-R_2)}{1-R_1R_2} \quad (s47)$$

$$I_{refl,\perp} = \frac{b(1-R_1)}{1-R_1R_2} \quad (s48)$$

which are the intensities of the transmitted and reflected cross-polarized light, respectively. Therefore

$$I_{refl,\perp} / I_{tran,\perp} = \frac{(1-R_1)b}{(1-R_1R_2)a + R_1(1-R_2)b} \quad (s49)$$

To compare the theoretical ratio predicted by Eq. (s49) with experiments, we can set $R_2 \approx R_1 = 0.30$, which leads to $I_{refl,\perp} / I_{tran,\perp} \approx 1.47$, in reasonably good agreement with our experimental value 1.69 (Fig. S3C at $\theta_i=0$). The predicted theoretical value of $I_{refl,\perp} / I_{tran,\perp}$, in the absence of the Fabry-Pérot effect, would be otherwise about 3.42.



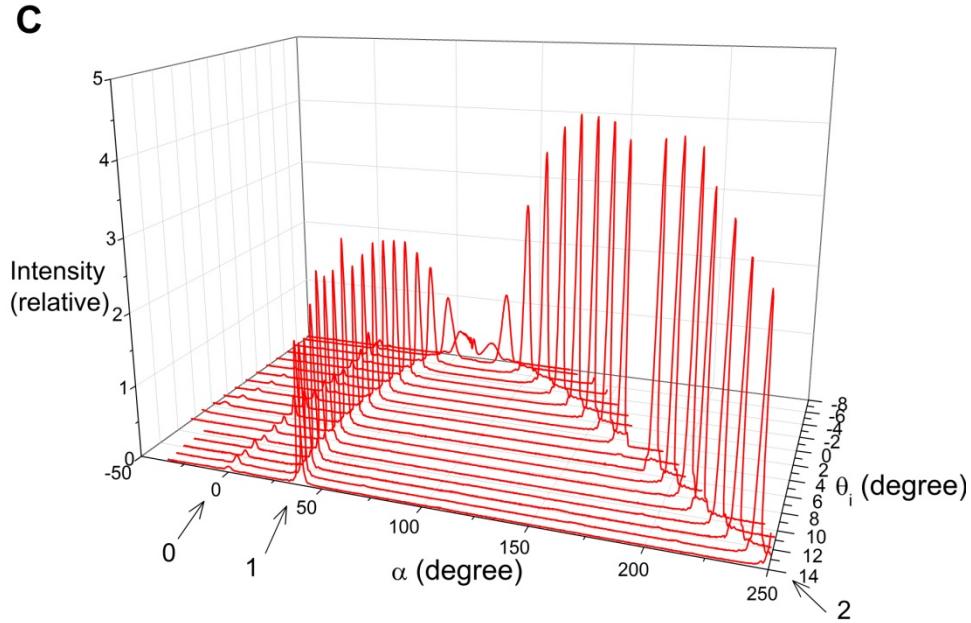


Fig. S1. (A) Schematic of the experimental setup for measuring far-field at different incident angles. (B) Measured far-field intensity as a function of the angular position of the mid-infrared detector α (defined in (A)) at different angles of incidence θ_i . The unit cell of the plasmonic interface has a lateral periodicity of $\Gamma = 15 \mu\text{m}$. Beams “0”, “1”, “2”, and “3” correspond to those labeled in (A). Beams “4” and “5” originate from the second-order diffraction of the periodic antenna array. At $\theta_i = 4.3$ degrees beam “2” cannot be measured in our setup because it is counter-propagating with the incident beam. (C) Measured far-field intensity profiles with a polarizer in front of the detector. The polarizer filters out the scattered light that is polarized perpendicular to the incident light.

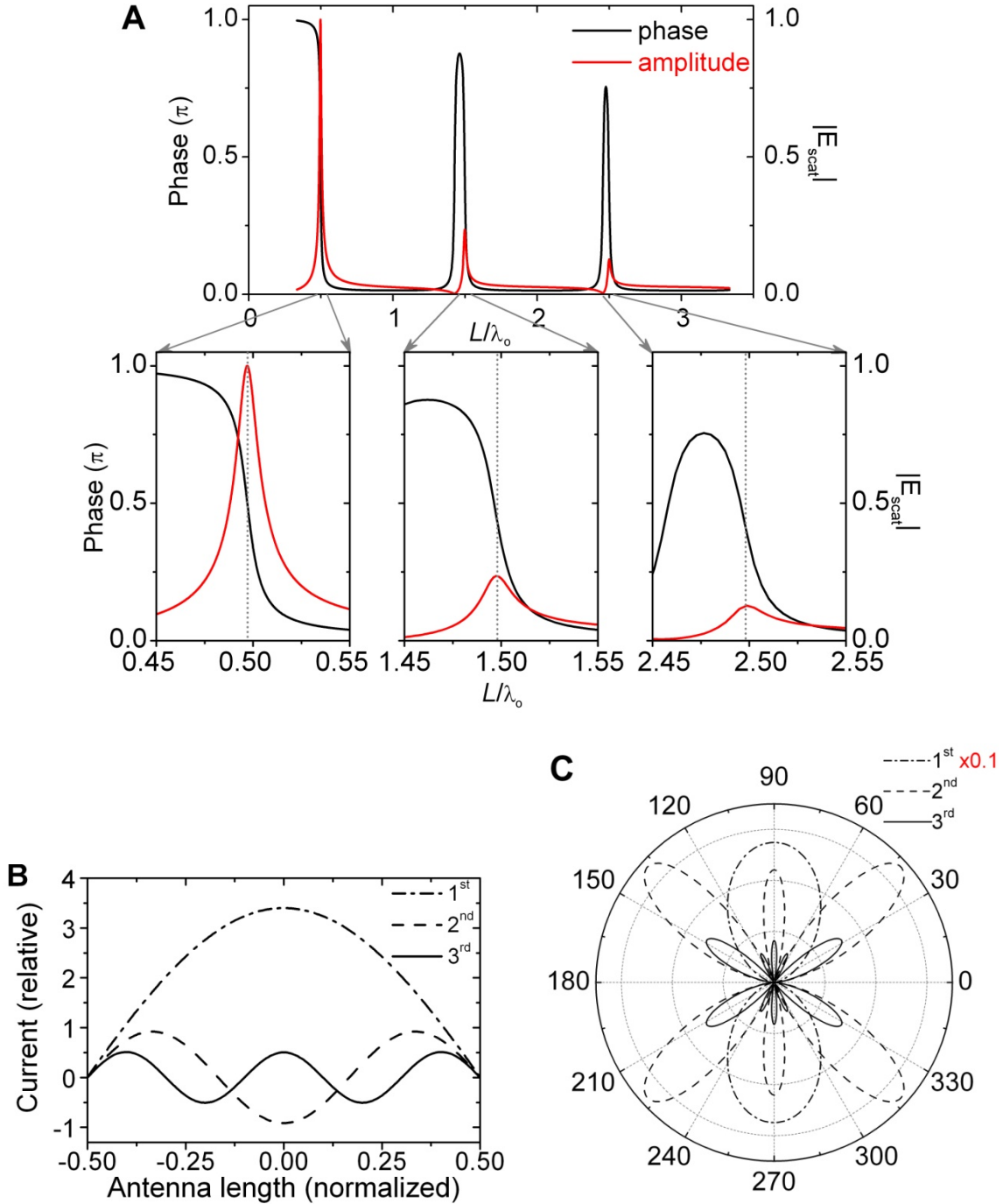


Fig. S2. (A) Upper panel: Phase and amplitude of scattered light from a straight rod antenna with a fixed length L and a high aspect ratio of 2000 (defined as rod length divided by rod diameter). The antenna is made of a perfect electric conductor and is in vacuum. The direction of incidence is normal to the antenna axis, and the incident polarization is along the antenna axis. The scattered light is monitored in a direction perpendicular to the antenna axis in the far-field. The antenna resonances are located at $L \approx m\lambda_0/2$, where m is an odd integer. Lower panels: Zoom-in views of the antenna's response in the vicinity of the three resonances. The vertical dotted lines indicate the

peaks of the amplitude response. **(B)** and **(C)** are current distributions and far-field radiation patterns ($|E|^2$) for the three resonances, respectively. The antenna is assumed to be oriented horizontally in **(C)**. For clarity, the radiation profile for the first-order resonance is demagnified by a factor of 10 in **(C)**.

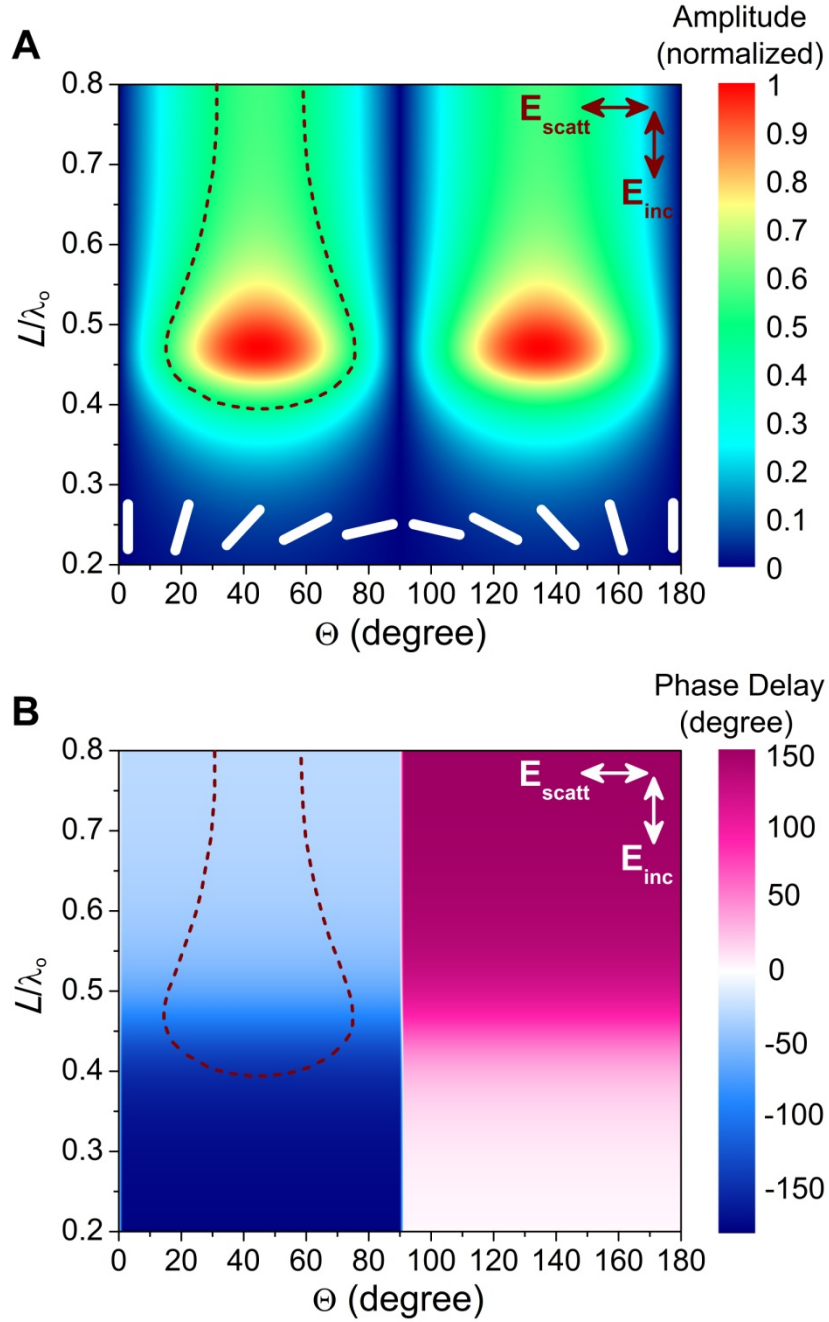


Fig. S3. (A) Amplitude of the cross-polarized radiation from a straight rod antenna as a function of the antenna length L and orientation Θ for monochromatic excitation at wavelength λ_0 . The antenna is in vacuum and has a radius $a = \lambda_0/100$. The dashed curve is an equal-amplitude contour. Schematics of antennas of various orientations are shown at the bottom of the figure. (B) Phase of the cross-polarized antenna radiation as a function of the antenna length L and orientation Θ .

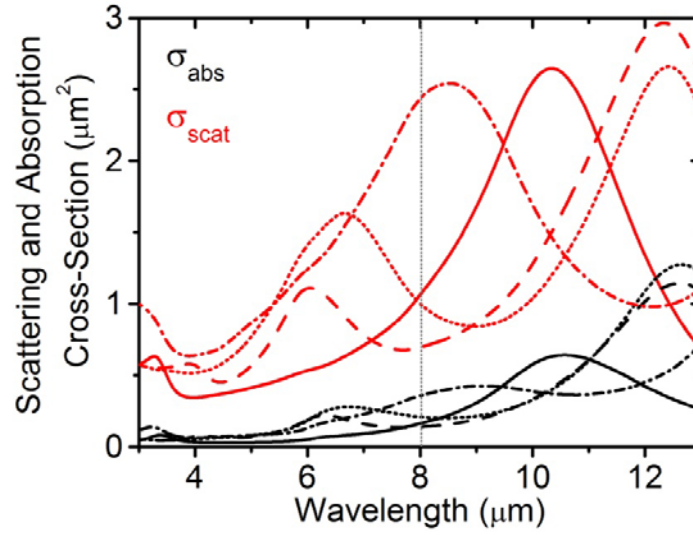


Fig. S4. Scattering (red curves) and absorption (black curves) cross-sections of V-antennas as a function of wavelength. Solid curves: length of antenna arms $h = 0.75 \mu\text{m}$, angle between antenna arms $\Delta = 180$ degrees; Dashed curves: $h = 0.94 \mu\text{m}$, $\Delta = 120$ degrees; Dotted curves: $h = 1.13 \mu\text{m}$, $\Delta = 90$ degrees; Dot-dashed curves: $h = 1.35 \mu\text{m}$, $\Delta = 60$ degrees. The vertical line indicates the operating wavelength.

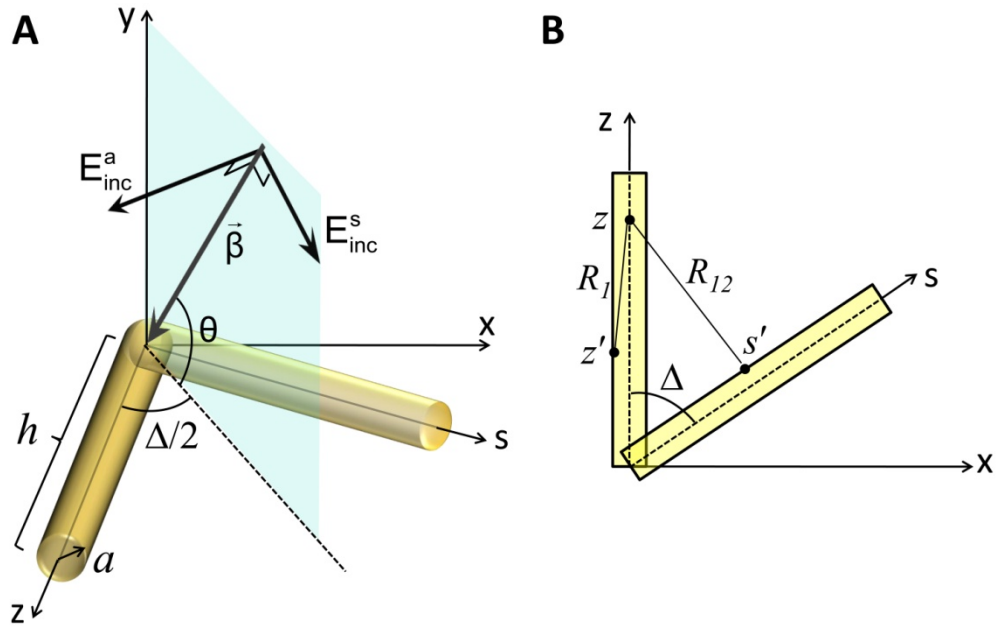


Fig. S5. (A) Schematics of the antenna geometry and excitation. The symmetry plane of the V-antenna is shown in light-blue. (B) Top view of the V-antenna.

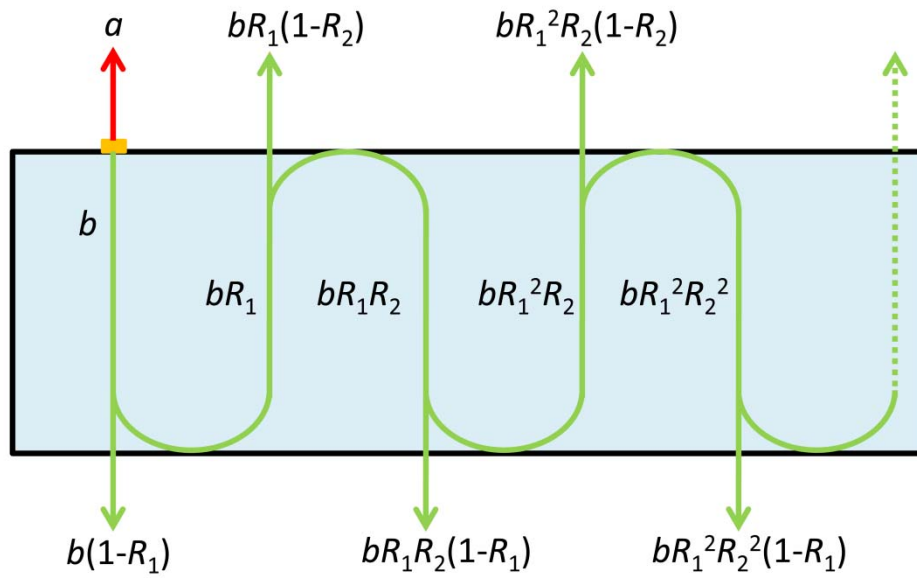


Fig. S6. Antenna radiations into the silicon slab undergo multiple reflections, leading to a modified ratio of intensity between the anomalous refraction and reflection as compared to that of an antenna array placed on the interface between two semi-infinite spaces.

Movie S1

Rotating spiral interference pattern created by tuning the optical path length of a reference beam relative to that of a vortex beam. The reference beam co-propagates with the vortex beam and its spherical-wave-like wavefront samples the helicoidal wavefront of the vortex beam, creating a spiral interference pattern. The intersection between the two wavefronts moves along the beam axis when the relative path length between the two beams is adjusted, producing a dynamically rotating spiral pattern.

References and Notes

1. J. B. Pendry, D. Schurig, D. R. Smith, Controlling electromagnetic fields. *Science* **312**, 1780 (2006). [doi:10.1126/science.1125907](https://doi.org/10.1126/science.1125907) [Medline](#)
2. U. Leonhardt, Optical conformal mapping. *Science* **312**, 1777 (2006). [doi:10.1126/science.1126493](https://doi.org/10.1126/science.1126493) [Medline](#)
3. W. Cai, V. Shalaev, *Optical Metamaterials: Fundamentals and Applications* (Springer, 2009)
4. N. Engheta, R. W. Ziolkowski, *Metamaterials: Physics and Engineering Explorations* (Wiley-IEEE Press, 2006).
5. I. I. Smolyaninov, E. E. Narimanov, Metric signature transitions in optical metamaterials. *Phys. Rev. Lett.* **105**, 067402 (2010). [doi:10.1103/PhysRevLett.105.067402](https://doi.org/10.1103/PhysRevLett.105.067402) [Medline](#)
6. S. D. Brorson, H. A. Haus, Diffraction gratings and geometrical optics. *J. Opt. Soc. Am. B* **5**, 247 (1988). [doi:10.1364/JOSAB.5.000247](https://doi.org/10.1364/JOSAB.5.000247)
7. R. P. Feynman, A. R. Hibbs, *Quantum Mechanics and Path Integrals* (McGraw-Hill, New York, 1965).
8. E. Hecht, *Optics* (3rd ed.) (Addison Wesley Publishing Company, 1997).
9. H. T. Miyazaki, Y. Kurokawa, Controlled plasmon resonance in closed metal/insulator/metal nanocavities. *Appl. Phys. Lett.* **89**, 211126 (2006). [doi:10.1063/1.2397037](https://doi.org/10.1063/1.2397037)
10. D. Fattal, J. Li, Z. Peng, M. Fiorentino, R. G. Beausoleil, Flat dielectric grating reflectors with focusing abilities. *Nat. Photonics* **4**, 466 (2010). [doi:10.1038/nphoton.2010.116](https://doi.org/10.1038/nphoton.2010.116)
11. J. A. Fan *et al.*, Self-assembled plasmonic nanoparticle clusters. *Science* **328**, 1135 (2010). [doi:10.1126/science.1187949](https://doi.org/10.1126/science.1187949) [Medline](#)
12. B. Luk'yanchuk *et al.*, The Fano resonance in plasmonic nanostructures and metamaterials. *Nat. Mater.* **9**, 707 (2010). [doi:10.1038/nmat2810](https://doi.org/10.1038/nmat2810) [Medline](#)
13. R. D. Grober, R. J. Schoelkopf, D. E. Prober, Optical antenna: Towards a unity efficiency near-field optical probe. *Appl. Phys. Lett.* **70**, 1354 (1997). [doi:10.1063/1.118577](https://doi.org/10.1063/1.118577)
14. L. Novotny, N. van Hulst, Antennas for light. *Nat. Photonics* **5**, 83 (2011). [doi:10.1038/nphoton.2010.237](https://doi.org/10.1038/nphoton.2010.237)
15. Q. Xu *et al.*, Fabrication of large-area patterned nanostructures for optical applications by nanoskiving. *Nano Lett.* **7**, 2800 (2007). [doi:10.1021/nl0713979](https://doi.org/10.1021/nl0713979) [Medline](#)
16. M. Sukharev, J. Sung, K. G. Spears, T. Seideman, Optical properties of metal nanoparticles with no center of inversion symmetry: Observation of volume plasmons. *Phys. Rev. B* **76**, 184302 (2007). [doi:10.1103/PhysRevB.76.184302](https://doi.org/10.1103/PhysRevB.76.184302)
17. P. Biagioni, J. S. Huang, L. Duò, M. Finazzi, B. Hecht, Cross resonant optical antenna. *Phys. Rev. Lett.* **102**, 256801 (2009). [doi:10.1103/PhysRevLett.102.256801](https://doi.org/10.1103/PhysRevLett.102.256801) [Medline](#)
18. S. Liu *et al.*, Double-grating-structured light microscopy using plasmonic nanoparticle arrays. *Opt. Lett.* **34**, 1255 (2009). [doi:10.1364/OL.34.001255](https://doi.org/10.1364/OL.34.001255) [Medline](#)

19. J. Ginn, D. Shelton, P. Krenz, B. Lail, G. Boreman, Polarized infrared emission using frequency selective surfaces. *Opt. Express* **18**, 4557 (2010). [doi:10.1364/OE.18.004557](https://doi.org/10.1364/OE.18.004557) [Medline](#)
20. Materials and methods are available as supporting material on *Science Online*.
21. J. F. Nye, M. V. Berry, Dislocations in wave trains. *Proc. R. Soc. Lond. A Math. Phys. Sci.* **336**, 165 (1974). [doi:10.1098/rspa.1974.0012](https://doi.org/10.1098/rspa.1974.0012)
22. M. Padgett, J. Courtial, L. Allen, Light's orbital angular momentum. *Phys. Today* **57**, 35 (2004). [doi:10.1063/1.1768672](https://doi.org/10.1063/1.1768672)
23. L. Allen, M. W. Beijersbergen, R. J. C. Spreeuw, J. P. Woerdman, Orbital angular momentum of light and the transformation of Laguerre-Gaussian laser modes. *Phys. Rev. A* **45**, 8185 (1992). [doi:10.1103/PhysRevA.45.8185](https://doi.org/10.1103/PhysRevA.45.8185) [Medline](#)
24. M. W. Beijersbergen, R. P. C. Coerwinkel, M. Kristensen, J. P. Woerdman, Helical-wavefront laser beams produced with a spiral phaseplate. *Opt. Commun.* **112**, 321 (1994). [doi:10.1016/0030-4018\(94\)90638-6](https://doi.org/10.1016/0030-4018(94)90638-6)
25. N. R. Heckenberg, R. McDuff, C. P. Smith, A. G. White, Generation of optical phase singularities by computer-generated holograms. *Opt. Lett.* **17**, 221 (1992). [doi:10.1364/OL.17.000221](https://doi.org/10.1364/OL.17.000221) [Medline](#)
26. H. He, M. E. J. Friese, N. R. Heckenberg, H. Rubinsztein-Dunlop, Direct observation of transfer of angular momentum to absorptive particles from a laser beam with a phase singularity. *Phys. Rev. Lett.* **75**, 826 (1995). [doi:10.1103/PhysRevLett.75.826](https://doi.org/10.1103/PhysRevLett.75.826) [Medline](#)
27. G. Gibson *et al.*, Free-space information transfer using light beams carrying orbital angular momentum. *Opt. Express* **12**, 5448 (2004). [doi:10.1364/OPEX.12.005448](https://doi.org/10.1364/OPEX.12.005448) [Medline](#)
28. D. M. Pozar, S. D. Targonski, H. D. Syrigos, Design of millimeter wave microstrip reflectarrays. *IEEE Trans. Antenn. Propag.* **45**, 287 (1997). [doi:10.1109/8.560348](https://doi.org/10.1109/8.560348)
29. J. A. Encinar, Design of two-layer printed reflectarrays using patches of variable size. *IEEE Trans. Antenn. Propag.* **49**, 1403 (2001). [doi:10.1109/8.954929](https://doi.org/10.1109/8.954929)
30. C. G. M. Ryan *et al.*, A wideband transmitarray using dual-resonant double square rings. *IEEE Trans. Antenn. Propag.* **58**, 1486 (2010). [doi:10.1109/TAP.2010.2044356](https://doi.org/10.1109/TAP.2010.2044356)
31. P. Padilla, A. Muñoz-Acevedo, M. Sierra-Castañer, M. Sierra-Pérez, Electronically reconfigurable transmitarray at Ku band for microwave applications. *IEEE Trans. Antenn. Propag.* **58**, 2571 (2010). [doi:10.1109/TAP.2010.2050426](https://doi.org/10.1109/TAP.2010.2050426)
32. H. R. Philipp, The infrared optical properties of SiO₂ and SiO₂ layers on silicon. *J. Appl. Phys.* **50**, 1053 (1979). [doi:10.1063/1.326080](https://doi.org/10.1063/1.326080)
33. R. W. P. King, *The Theory of Linear Antennas* (Harvard University Press, 1956).
34. J. D. Jackson, *Classical Electrodynamics* (3rd edition) (John Wiley & Sons, Inc. 1999) pp. 665.
35. E. D. Palik, *Handbook of Optical Constants of Solids* (Academic Press, 1998).

36. I. Puscasu, D. Spencer, G. D. Boreman, Refractive-index and element-spacing effects on the spectral behavior of infrared frequency-selective surfaces. *Appl. Opt.* **39**, 1570 (2000). [doi:10.1364/AO.39.001570](https://doi.org/10.1364/AO.39.001570) [Medline](#)
37. G. W. Hanson, On the applicability of the surface impedance integral equation for optical and near infrared copper dipole antennas. *IEEE Trans. Antenn. Propag.* **54**, 3677 (2006). [doi:10.1109/TAP.2006.886516](https://doi.org/10.1109/TAP.2006.886516)
38. C. R. Brewitt-Taylor, D. J. Gunton, H. D. Rees, Planar antennas on a dielectric surface. *Electron. Lett.* **17**, 729 (1981). [doi:10.1049/el:19810512](https://doi.org/10.1049/el:19810512)
39. D. B. Rutledge, M. S. Muha, Imaging antenna arrays. *IEEE Trans. Antenn. Propag.* **30**, 535 (1982). [doi:10.1109/TAP.1982.1142856](https://doi.org/10.1109/TAP.1982.1142856)

Acknowledgements: The authors acknowledge helpful discussion with J. Lin, R. Blanchard, and A. Belyanin. The authors acknowledge support from the National Science Foundation, Harvard Nanoscale Science and Engineering Center (NSEC) under contract NSF/PHY 06-46094, and the Center for Nanoscale Systems (CNS) at Harvard University. Z. G. acknowledges funding from the European Communities Seventh Framework Programme (FP7/2007-2013) under grant agreement PEOF-GA-2009-235860. M.A.K. is supported by the National Science Foundation through a Graduate Research Fellowship. Harvard CNS is a member of the National Nanotechnology Infrastructure Network (NNIN). The Lumerical FDTD simulations in this Letter were run on the Odyssey cluster supported by the Harvard Faculty of Arts and Sciences (FAS) Sciences Division Research Computing Group.